MEMS Components for NMR Atomic Sensors

Radwan M. Noor , *Student Member, IEEE*, and Andrei M. Shkel , *Fellow, IEEE*

Abstract—This paper introduces a batch fabrication method to manufacture micro-electromechanical system (MEMS) components for nuclear magnetic resonance (NMR) atomic sensors, such as NMR gyroscope (NMRG) and NMR magnetometer (NMRM). The components presented are: 1) micro-coils generating the magnetic field with the magnetic field homogeneity of $H = 354$ ppm; 2) spherical micro-fabricated atomic cells confining alkali metal and noble gases; 3) micro-heaters keeping the alkali metal in a vapor state while minimizing residual magnetic fields; and 4) origamilike silicon structures with integrated optical reflectors preserving 90.9% of the light polarization. The introduced design utilized a glassblowing process, origamilike folding, and a more traditional MEMS fabrication. We presented an analytical model of imperfections, including errors associated with micro-fabrication of MEMS components. In light of the developed error model, phenomenological dynamic model describing NMR sensors, and experimental evaluation of components, we predicted the effect of errors on performance of NMRG and NMRM. We concluded that with a realistic design, a 5-mrad angular misalignment between coils and folded mirrors, and a 100-μm linear misalignment between folded coils, it would be feasible to achieve an NMRG with ARW 0.1 deg/rt-hr and an NMRM with sensitivity on the order of 10 fT/rt-Hz.   [2018-0169]

Index Terms—Atomic sensors, microfabrication, nuclear magnetic resonance (NMR), NMR gyroscopes, NMR magnetometers.

I. INTRODUCTION

ATOMIC sensors can deliver a precise measurement of physical quantities such as time, magnetic field, and rotation by utilizing a cloud of conditioned atoms [2]. For example, in table-top setups, an atomic magnetometer can measure magnetic fields with a sensitivity of $1 \ fT/\sqrt{Hz}$ [3], and an atomic gyroscope can measure rotation with an Angle Random Walk (ARW) of 0.002 deg$\sqrt{hr}$ [4]. The emerging applications that demand low-cost chip-scale atomic sensors [5], [6] have started a trend in the early 2000s on miniaturization of atomic sensors and their components. The advancements in miniaturized cell fabrication [7]–[10],

A. M. Shkel is with the Microsystems Laboratory, Department of Mechanical and Aerospace Engineering, Department of Electrical Engineering and Computer Sciences, and the Department of Biomedical Engineering, University of California at Irvine, Irvine, CA 92697 USA (e-mail: ashkel@uci.edu).

R. M. Noor is with the Microsystems Laboratory, Department of Electrical Engineering and Computer Science, University of California at Irvine, Irvine, CA 92697 USA (e-mail: rmmohamm@uci.edu).

Color versions of one or more of the figures in this paper are available online at http://ieeexplore.ieee.org.

Digital Object Identifier 10.1109/JMEMS.2018.2874451

and Vertical Cavity Surface Emitting Lasers (VCSELs) [11], encouraged developments towards miniaturization of atomic clocks [12], atomic magnetometers (NMRMs) [13]–[15], and atomic gyroscopes (NMRGs) [15]–[17].

The process of conditioning atoms for atomic sensors (such as NMRM and NMRG) consists of multiple steps. The first step is to confine the atomic cloud in a container, i.e., a vapor cell. The next step is to heat the cell, which is necessarily to vaporize the alkali metal and to increase the vapor pressure, which would effectively increase the signal-to-noise ratio of measurement. This is followed by aligning the atomic spins of nuclei by applying a precise static and oscillating magnetic fields via electromagnetic coils. The next step is to optically polarize the spins using a laser source, assuring that their magnetic moments are aligned forming a net magnetization vector. Lastly, in the case of NMRG, the sensor is encapsulated using a μ-metal shield to preserve this conditioning during sensor operation. In the case of NMRM, no magnetic shield would be typically used.

The utilization of Micro-ElectroMechanical Systems (MEMS) techniques accelerated the advancement of miniaturization of atomic cells [18]–[20]. However, MEMS techniques have not been adopted widely for other essential components of atomic sensors, such as multi-axis magnetic field coils, cell heaters, and optical components. In previous studies [15], [21], multi-axes coils and cell heaters were realized through flexible printed circuit boards technique. Individually machined optical apparatus, such as lenses and light reflectors, were assembled to route the light in-and-out of the cell [21], [22]. One obvious limitation of such techniques is that the components were picked and placed individually, which made the assembly process inefficient and devices bulky. MEMS techniques offer an approach to address this limitation by utilizing a lithography driven batch fabrication.

In our previous work [1], we introduced a miniaturization method based on the micro-fabrication of NMR components on a wafer-level, as a potential approach for size, weight, power, and cost (SWaP+C) reduction. Our method combines micro glassblowing technology for fabrication of miniaturized atomic cells [18], and a 3-D folded MEMS structures [23], for fabrication of magnetic coils, interconnects, silicon backbones, and light reflectors. However, miniaturization comes with a cost of imperfections. In this work, we discuss and analyze the contribution of errors introduced by each component on the overall performance of NMR atomic sensors. We then demonstrate that MEMS-based implementation is a potential candidate for precision sensing.

This paper is structured as follows. In Section II, we described the principle of operation and listed the essential building blocks of atomic sensors. Then, in Section III,
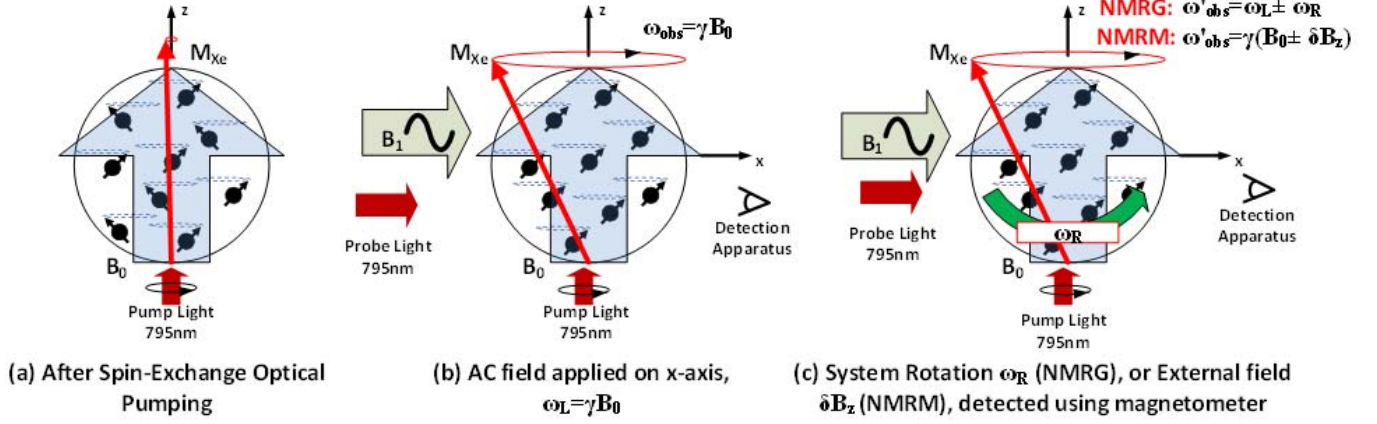
Fig. 1. Principle of operation of Nuclear Magnetic Resonance Gyroscopes and Magnetometers, (a) due to optical pumping and spin exchange, the atoms are precessing around the applied field and are aligned, resulting in a net magnetization vector in the z-direction, (b) the applied oscillating field B_1 synchronizes the atoms' spins in phase, so that the magnetization vector is precessing around B_0 with a frequency ω_L, (c) a frequency shift is observed after applying the rotation rate ω_R (in case of gyroscope) or after applying a variable external magnetic field (in case of magnetometer). The illustration is adopted from [24].

we introduced a set of phenomenological equations that described the ideal dynamics of spin-polarized devices. In Section IV, we present our suggested miniaturized implementation of NMRG and NMRM using the micro-fabrication techniques. Section V presents an analytical model supported with experimental evaluation of sources of the fabrication imperfection. Finally, Section VI talks about the projection of assembly errors on the device performance based on the developed model. Section VII concludes the paper and gives an outlook on the development of MEMS-based atomic sensors.

II. ESSENTIAL BUILDING BLOCKS

In this section, the principle of operation of the NMR-based sensors is briefly explained, followed by an overview of the essential building blocks required for realization of such systems.

A. Principle of Operation

The configuration for NMR gyroscopes and magnetometers is designed to detect a response of a cloud of alkali metal (for example, Rb) vapor and a noble gas (for example, Xe) to rotation or a magnetic field. It should be noted that other alkali metals and noble gases can be used, for example K and He. The cloud of atoms is conditioned and interrogated electromagnetically and optically to detect the phenomenon of interest (rotation or magnetic field). When Xe atoms are in an applied magnetic field B_0 along the z-axis, Fig. 1, they develop a precessing motion around the axis of the applied field with a certain angular frequency (Larmor frequency), such that

$$\omega_{obs} = \omega_L = \gamma B_0, \qquad (1)$$

where γ is the gyromagnetic ratio, which is a unique value for each atomic species. For example, for ^{129}Xe atoms $\gamma = 11.86$ Hz/μT [25]. A spin-exchange optical pumping process is used to align Xe atoms, Fig. 1-(a) [26]. In this process, a circularly polarized light beam polarizes (pumps) the Rb atoms. Circularly polarized light is fundamental for the optical pumping process because it has angular momentum

which can change the quantum state of the outer electrons of the Rb atoms to reach the pumped state ($m_F = -2$ or $m_F = 2$ by the right or left handed polarized light, respectively) [24]. Then, direct collisions and formation of Van Dar Waals molecules (spin exchange) transfer the polarization from Rb atoms to Xe atoms. This process adds up the magnetic moments of Xe atoms to form a net magnetization vector. An applied oscillating field B_1 at Larmor frequency along the x-axis synchronizes the atoms in phase, so that the effective magnetization vector precesses around the B_0 magnetic field with a frequency ω_L, Fig. 1-(b).

For the NMR gyroscope, when a rotation rate ω_R is applied to the whole system, the new observed frequency of the magnetization vector precession becomes

$$\omega'_{obs} = \omega_L \pm \omega_R \qquad (2)$$

This phenomenon is illustrated in Fig. 1-(c).

The behavior of the Xe magnetization vector is transferred to the ensemble of Rb atoms through the same process of spin exchange. Subsequently, the Rb atoms are detected via a linearly polarized light. The rotational rate can be then extracted from the frequency measurements.

The principle of operation for NMR magnetometer is similar to that of the NMR gyroscope. However, instead of detecting the applied rotational rate ω_R, NMR magnetometers detect the changes in the magnetic field along the z-axis, Fig. 1. The observed frequency of the magnetization vector becomes

$$\omega'_{obs} = \gamma \left(B_0 \pm \delta B_z \right) \qquad (3)$$

B. Basic Components

Fig. 2 shows a diagram of the components required for NMR sensors. The atomic vapor cell is in the heart of the NMR sensors and encloses the noble gas and the alkali metal atoms. Alkali metals are usually in a solid-state at the room temperature and a cell heater is needed to raise temperature in order to vaporize the metal. Vaporization leads to increase in the alkali vapor density. Multi-axis magnetic field coils are needed to apply the static magnetic field B_0 along one
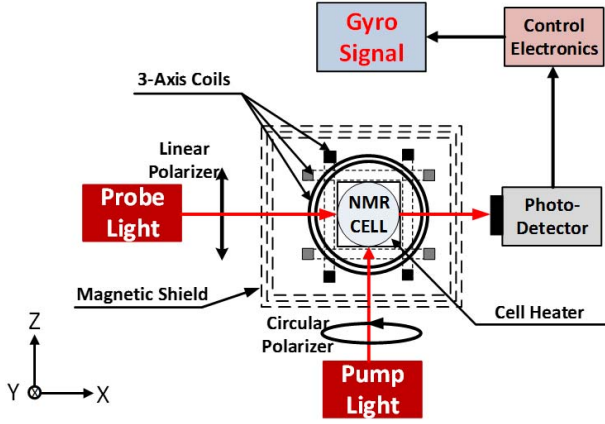
Fig. 2.   Functional elements of Nuclear magnetic resonance gyroscope.

Fig. 3.   Typical response of equations (4) and (5), showing the absorption (v-mode) and dispersion (u-mode).

Fig. 4.   An implementation of NMR atomic sensors.

axis, the oscillating field B_1 along a perpendicular axis, and an additional field along the third axis might be needed to cancel any residual fields inside the cell. Light sources and photo-detectors are needed for pumping and detecting the precessing alkali atoms. Optics, such as mirrors, lenses, and linear and circular polarizers are required to collimate the light, ensuring a proper polarization of the beams (circular and linear polarization for the pump and probe beams, respectively). NMR sensors are sensitive to small magnetic fields, on the order of nano-Tesla. Knowing that the surrounding fields, such as the Earth's magnetic field, can be 3 to 4 orders of magnitudes larger, an NMRG requires a magnetic shield to eliminate those ambient fields. In the case of NMRM no magnetic shield would be typically used. Finally, a set of control electronics that controls the fields and extracts the precession of the magnetization vector from the photo-detector signal is necessary [27].

III. PHENOMENOLOGICAL DESCRIPTION

In this section, we introduce a phenomenological mathematical model of NMR sensors. The change of the magnetization vector in an applied magnetic field was described by the mathematical model developed by Bloch [28] 1946. Under the assumptions of an applied static magnetic field B_0 on the z-axis, an oscillating magnetic field $B_x = B_1 \cos(\omega_a t)$ is applied along the x-axis and $B_y = \mp B_1 \sin(\omega_a t)$ is applied along the y-axis. Assuming that the input rotation is small, the analytical solution is found to be,

$$u = M_0 \frac{\gamma B_1 T_2^2 \Delta\omega}{1 + (T_2 \Delta\omega)^2 + (\gamma B_1)^2 T_1 T_2}, \qquad (4)$$

$$v = M_0 \frac{\gamma B_1 T_2}{1 + (T_2 \Delta\omega)^2 + (\gamma B_1)^2 T_1 T_2}, \qquad (5)$$

$$M_z = M_0 \frac{1 + (T_2 \Delta\omega)^2}{1 + (T_2 \Delta\omega)^2 + (\gamma B_1)^2 T_1 T_2}, \qquad (6)$$

where $\Delta\omega = (\gamma B_0 - \omega_a) - \omega_R$ is a mismatch between the applied oscillating field and the Larmor frequency of the atoms $\omega_L = \gamma B_0$, T_1 and T_2 are the longitudinal and transverse relaxation time constants, respectively, and (u, v) are the magnetization vector components projected on a rotating
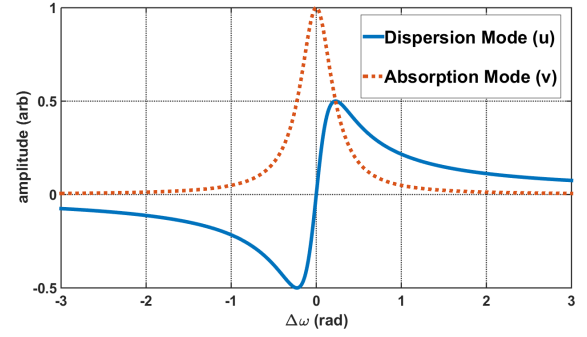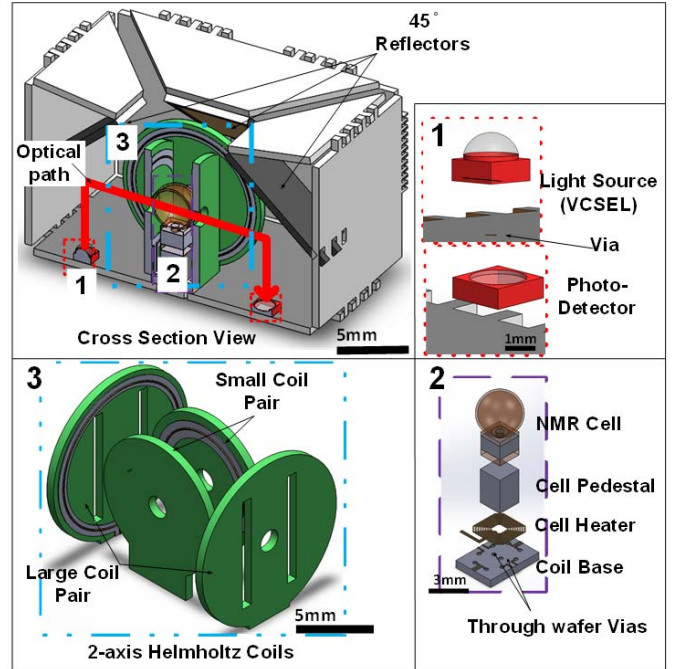
coordinate system that rotates around the z-axis. The component u will rotate in phase with B_1, while v will rotate in quadrature with B_1. Derivation of equations (4), (5) and (6) can be found in [28].

If we set the oscillating field frequency exactly at the Larmor frequency, then the rotational rate ω_R can be extracted from either the absorption mode (v) or the dispersion mode (u). A typical normalized response described by equations (4) and (5) is shown in Fig. 3, where it can be noted that the dispersion mode is more suitable to distinguish the direction of rotation.

IV. MINIATURIZATION

In this section, we introduce our implementation of NMR sensors. We start with explaining the approach of combining the 3-D folded MEMS and a micro-glass blowing techniques. Next, we introduce the fabrication processes of each component and demonstrate fabricated prototypes. Our miniaturized implementation of NMR atomic sensors is sketched in Fig. 4.
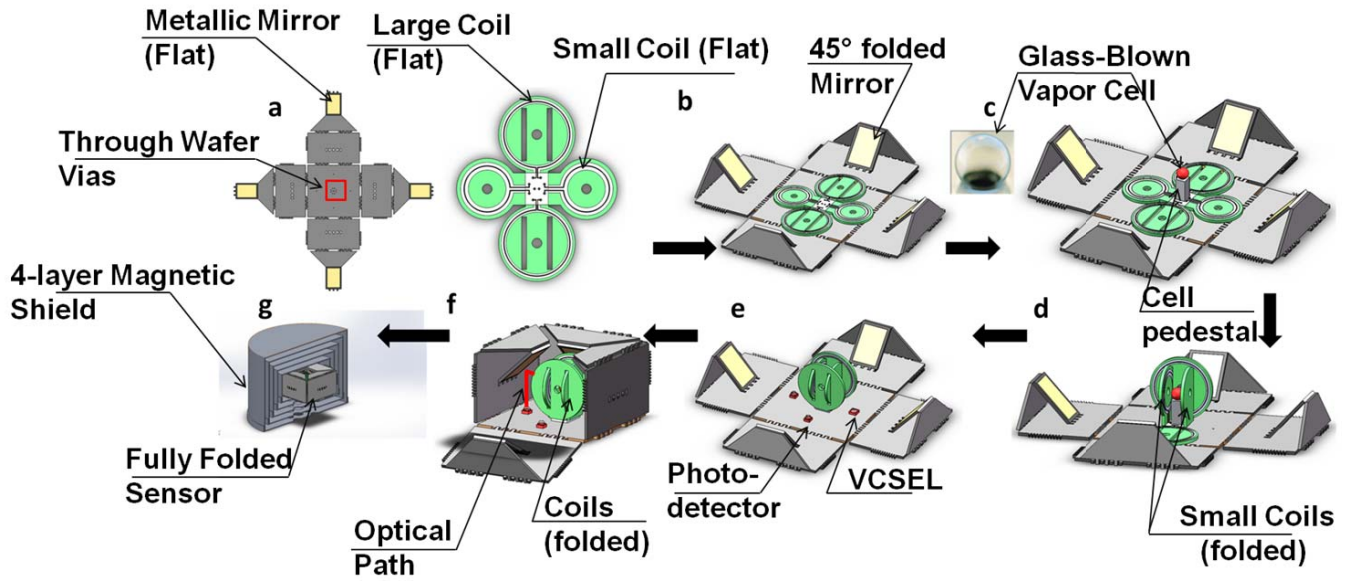
Fig. 5. Conceptual drawing of the folded micro-NMRG. (a) Double-folded structure and coils fabricated on a flat wafer, (b) Initial folding of backbone structure with co-fabricated mirrors, (c) Assembly of glassblown micro cell, (d) Coils are folded, (e) VCSELs and photo-detectors are assembled, (f) Backbone structure is fully folded, (g) The sensor is placed inside magnetic shields (a cross-section view of the shields).

The atomic cell is a glassblown micro-sphere filled with Rb, Xe, and a buffer gas, for example N_2 and Ne, positioned on top of a cell heater and surrounded by two orthogonal pairs of Helmholtz coils. This assembly is encapsulated by a foldable backbone structure that houses 2 VCSEL's and 2 photo-detectors, all connected by through-wafer-vias to the outer-side of the backbone structure. Four 45° reflectors are included in the design of the backbone structure that route the light beams from VCSEL's through the cell to the photo-detectors. A 4-layer μ-metal shield protects the sensor form surrounding magnetic interferences (not shown).

Our approach starts with fabrication of a backbone, which is a double-folded structure with integrated reflectors and Helmholtz coils on a flat silicon wafer, Fig. 5-(a). Then, the metallic reflectors are folded, and subsequently the coils are assembled in the middle of the backbone structure, Fig. 5-(b). Next, the atomic cell is assembled in the middle of the folded Helmholtz coils, Fig. 5-(c). After folding the coils, two Vertical Cavity Surface Emitting Lasers (VCSEL) and two photo-detectors are assembled, Fig. 5-(d, e). The backbone structure is finally folded and placed inside multi-layer magnetic shields, Fig. 5-(f, g). The fabrication process and the design descriptions for each of these components are discussed next.

The assembly of the folded coil and the glassblown cell in the middle of the folded structure is achieved via pick and place technique. Several alternative folding approaches were also explored, including a self-assembly triggered either by light, magnetic field, or resistive heating actuation of shape memory polymers [29]–[31]. However, due to compatibility issues of those polymers with our wafer-level process and the sensor operation, we adopted a guided assembly technique using a folding mold, Fig. 6. This folding method is compatible with a wafer-level assembly process.
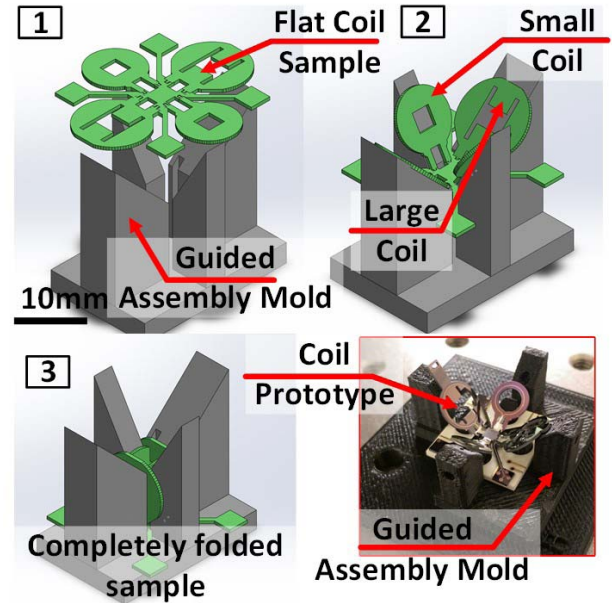

Fig. 6. Sketch of the guided assembly process of the folded Helmholtz coils using a pre-defined mold, insert: a picture of a coil's sample inside a folding mold prototype created using 3D printing.

A. Folded Helmholtz Coils and Integrated Cell Heater

The fabrication process of the folded coils with integrated cell heater starts with a 500μm silicon wafer coated with 3000Å of LPCVD silicon nitride, Fig. 7-(a). The first metal layer of the cell heater was defined by evaporating 500/5000Å Cr/Au, followed by photo-lithography and wet metal etching using Cr TFE and Au GE8110 etchants from Transene Company for etching Cr and Au respectively, Fig. 7-(b). Note that a lift-off process can be used at this step.
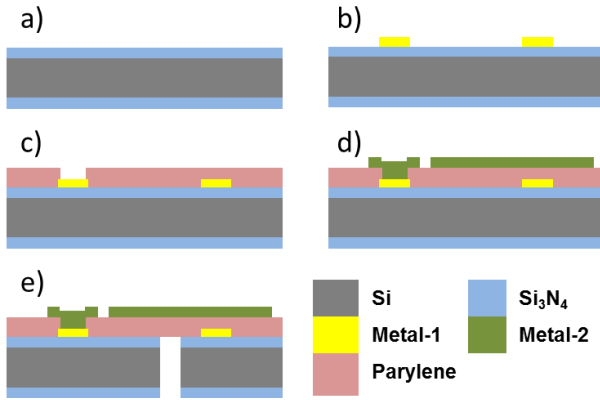
Fig. 7. Fabrication process of the folded Helmholtz coils.

Fig. 8. Heater layout illustrating the (+−−+−++−) configuration. Sign convention, (+) is for counter clockwise and (−) for clockwise flow of current in the heater traces.

Fig. 9. Fabricated sample of the folded Helmholtz coils: in the flat state (left), and in the folded state (right).

Next, a 14μm parylene film was deposited on top of metal-1, and subsequently etched using reactive ion etching (RIE) with a 1000Å Ti film as the hard mask, forming the flexible hinges, Fig. 7-(c) [32]. Metal-2 was an evaporated and patterned 500/2500Å Cr/Au layer to form the Helmholtz coil traces, as shown in Fig. 7-(d). Finally, the coils and hinges were defined using photo-lithography, followed by RIE-DRIE-RIE etching sequence of the Si_3N_4-Si-Si_3N_4 layers, respectively, starting from the backside of the wafer, Fig. 7-(e).

The generated field by an ideal Helmholtz coil at the center of the coil along the axis is a superposition of the field generated by two current loops separated by a distance equal to the radius of a single loop [33],

$$B_z = \frac{\mu_0 N I R^2}{2\left[(z - R/2)^2 + R^2\right]^{3/2}} + \frac{\mu_0 N I R^2}{2\left[(z + R/2)^2 + R^2\right]^{3/2}},$$

(7)

where μ_0 is the air permeability, N is the number of turns, R is the coil's radius. The field homogeneity is defined as

$$\eta_{B_z(ppm)} = \frac{\Delta B_z}{B_0} \times 10^6,$$

(8)

where ΔB_z is the difference between the field maximum and minimum across the cell, B_0 is the field value at the center of the coil.

The trade-offs in the coil's design are the size and homogeneity, both can be determined by the radius of the coil according to equations (7) and (8). The field homogeneity improves as the coil's radius increases relative to the cell. However, for a 1mm cell a coil of radius above 5mm does not provide a significant improvement in the magnetic field homogeneity, but increases volume of the coil [33]. For example, homogeneity of an ideal Helmholtz coil with the radii of 3mm, 5mm, and 6mm across 1mm cell would be around 860ppm, 113ppm, and 55ppm, respectively. A coil of radius of 4.2mm was chosen for our design.

The heater design utilized a multi-pole current carrying conductors with (+ − − + − + + −) configuration, illustrated in Fig. 8. This created a 2^3 poles magnetic moment that resulted in a suppressed magnetic field from the heating current [34]. In addition to using a magnetic field suppressing
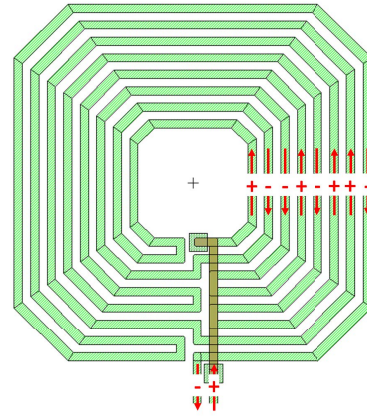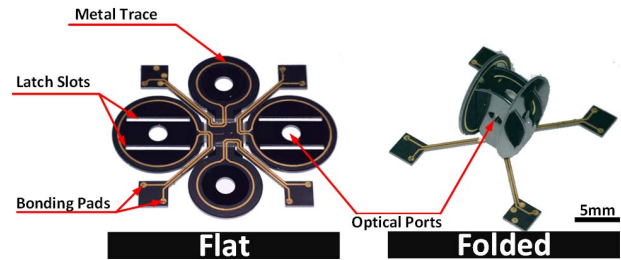
heater layout, a modulated heater current with a frequency of 100kHz was utilized (the frequency was intentionally selected far away from Xe resonance frequencies of ~100Hz to reduce an interference with Xe precession). The heater was placed 4.2mm below the cell and a thermally conductive micro-pedestal made from silicon was used to interface the cell to the heater. This distance was chosen to ensure placement of the cell at the center of symmetry coils and placement of the heater at the base of the coils, Fig. 4-(2).

B. Glassblown Atomic Vapor Cell

Our approach utilizes a glassblowing process for manufacturing spherical micro-cells [18]. A perceived advantage of spherical cells is their 3-axes symmetry and ability to have two or more optical ports, which is required for NMRG and NMRM operation. The presented process allows filling, with alkali metal, noble gas, and buffer gas, multiple cells at the same time providing a control over the Rb gas pressure inside the cell, regardless of the cell size. The process started with the DRIE etching of 750μm-deep cavities in a 1mm-thick Si-wafer, Fig. 10-(a). The first anodic bonding of a 500μm-thick Pyrex-wafer to the Si-wafer sealed the cavities at atmospheric pressure. After placing the wafer-stack in a furnace at ~850°C for 5-7 minutes, spherically shaped glass shells were formed [18], Fig. 10-(b). At the next step of the process the backside of Si was opened and ~250μm-deep micro-channels were defined by DRIE; the micro-channels after this step are shown in Fig. 10-(c). The second anodic
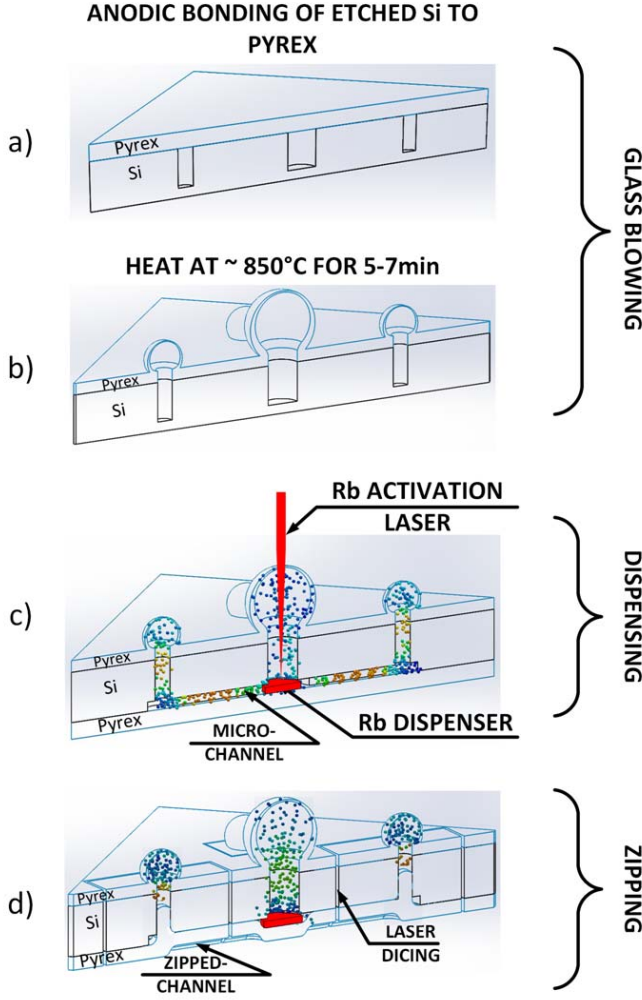
Fig. 10. Description of the process flow: (a) Sealing cavities in Si by anodic bonding of glass wafer to etched Si wafer, (b) glassblowing of cells, (c) Filling with alkali, noble gas, and buffer gas, (d) Closing channels between dispensing and satellite cells, followed by dicing.
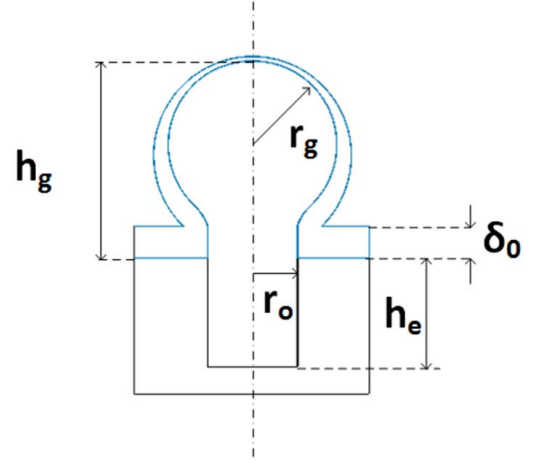

Fig. 11. Sketch of a cross section view of the glassblown cell.

are given by equations (9) and (10), respectively [36]

$$h_g = \frac{\left[\left(3V_g + \sqrt{r_o^6\pi^2 + 9V_g^2}\right)\pi^2\right]^{2/3} - r_o^2\pi^2}{\pi\left[\left(3V_g + \sqrt{r_o^6\pi^2 + 9V_g^2}\right)\pi^2\right]^{1/3}} \tag{9}$$

$$r_g = \frac{h_g^2 + r_o^2}{2h_g} \tag{10}$$

where V_g is the inner volume of the cell equal to $h_e\pi r_o^2(T_f/T_s - 1)$, T_f and T_s are the glass blowing furnace and the cavity sealing temperatures in Kelvins, r_0 is the radius of the etched cavity, h_e is the etched cavity depth [36]. An experimental validation of this process showing the Rb absorption curve was presented in our previous work [1].

C. Folded Structure

The backbone of folded NMR sensors was fabricated using a process similar to the one used for coils, but with only one metal layer. The process is implemented on a 4-inch silicon wafer, but can be adopted for larger sizes. Flexible parylene hinges were defined on one side of the wafer, a metal layer of 500/5000Å Cr/Au was evaporated and patterned to form the metal reflectors on the other side of the wafer. The fabricated prototype of the double folded structure is shown in Fig. 12, with one of the two optical paths illustrated.

The folded structure is the backbone of the sensor and the light reflectors integrated within. The design consideration is to provide four 45° reflectors in a compact design that route the pump and probe beams in and out of the cell. The angle of each reflector is determined by three panels that construct each side wall of the folded structure, the required relative angles between the panels to achieve 45° reflectors are listed in Table I. The reflector panel was designed to be 8×6mm to provide a mechanical support of the side wall and to ensure a large enough area for beam routing.

V. MODELING AND EXPERIMENTAL EVALUATION

In this section, we introduce our analytical model for errors associated with 3D folding process, such as misalignment of

bonding took place after alkali pills were placed in the central cell (alkali pills are Rb dispensers supplied by SAES getters). The cells are subsequently transferred and anodically bonded in a chamber with a noble gas and a buffer gas at a pressure of 410 Torr (Xe: 65 torr, Ne: 45 Torr, and N_2: 300 Torr). After the bonding process was completed, each pill was activated by focusing a 1-1.5W laser for 2 minutes, which released the alkali vapor to the satellite cells, [35], Fig. 10-(c). After dispensing, the channels and the cells were sealed, Fig. 10-(d). This was accomplished by localized heating of the glass layer with a laser, which sucked-in the softened glass in the below-atmospheric-pressure channels and cells. The glass cooling permanently sealed the channels and plugged the cells' post, isolating the cells and assuring a necessary level of cell sphericity. Finally, a pulsed laser was used to dice cells across the sealed channels.

The design parameters that control the glass blown cell's volume are the radius and depth of the etched Si cavities (cylindrical cavities are preferred for axissymmetric cells). The hight h_g and the inner radius of the cell r_g, shown in Fig. 11,
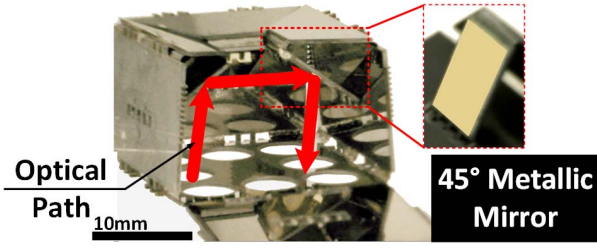
Fig. 12. Fabricated folded structure with 45° metallic reflectors. Only one optical path is shown.

components after folding and reinforcement against shock, vibration or thermal expansion. The analytical model was evaluated by experimental validation of each component. The fabrication process utilized lithography-based machining accuracy to define dimensions of the micro-components in 2-D. However, folding those components into a 3-D configuration introduced assembly errors. The considered components in this analysis were the folded Helmholtz coils and the double-folded backbone structure.

In calculating homogeneity, the volume of interest was a 1mm diameter glass blown cell placed at the center of the two coils.

A. Folded Helmholtz Coil

1) Analytical Model: An Ideal Helmholtz coil consists of two identical current loops separated by a distance equal to the radius of each loop. Assuming there are two current loops perpendicular to the z-axis, with radius r_{coil} and their centers at locations of $(0, 0, -r_{coil}/2)$ and $(0, 0, r_{coil}/2)$. The field generated by this Helmholtz coil at any point (x,y,z) can be calculated using the Biot-Savart law as

$$\vec{B}_{HH}(x, y, z) = \vec{B}_1(x, y, z + r_{coil}/2) + \vec{B}_2(x, y, z - r_{coil}/2), \quad (11)$$

A model developed in [37] was adopted here to study the level of accuracy required for the folding process.

Misalignment errors in the structure are either due to the angular or linear shift of one current loop with respect to the other. To simplify the model, we assumed that the total misalignment is a superposition of angular and linear misalignments by each loop of the coil.

There are two angles of misalignment, as shown by the loop on the left of Fig. 13: α_z is the angle of the loop with the y-axis and β_z is the angle with the x-axis. The loop's field due to the angular misalignments is

$$\vec{B}_1 = \vec{B}(u - u_0, v - v_0, w - w_0), \quad (12)$$

where $(\hat{u}, \hat{v}, \hat{w})$ is a rotated coordinate frame and is related to the main frame $(\hat{x}, \hat{y}, \hat{z})$ as

$$\begin{bmatrix} \hat{u} \\ \hat{v} \\ \hat{w} \end{bmatrix} = [T_z(\alpha_z, \beta_z)] \times \begin{bmatrix} \hat{x} \\ \hat{y} \\ \hat{z} \end{bmatrix}, \quad (13)$$
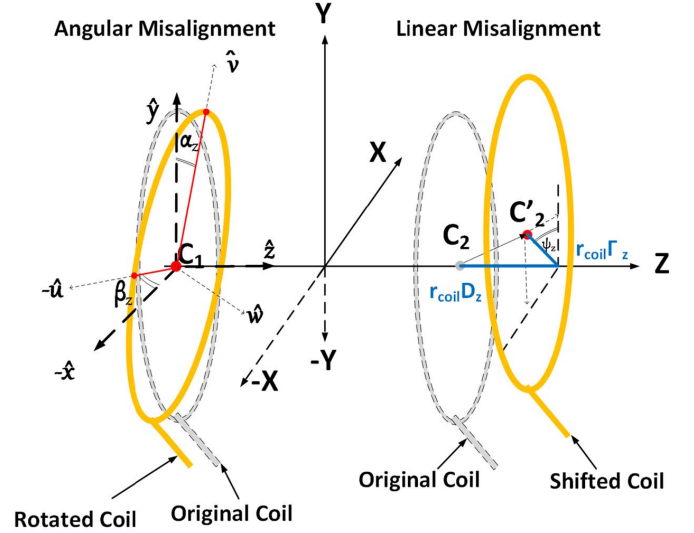

Fig. 13. Sketch of angularly (left) and linearly (right) misaligned coils, (original location of the coils is illustrated with dashed lines and gray color).

where T_z is the rotation matrix [37], and is defined as

$$\begin{bmatrix} -\cos\beta_z & -\sin\alpha_z \cos\alpha_z \sin\beta_z & \cos^2\alpha_z \sin\beta_x \\ 0 & \cos\alpha_z & \sin\alpha_z \\ \cos\alpha_z \sin\beta_z & -\sin\alpha_z \cos\beta_z & \cos\alpha_z \cos\beta_z \end{bmatrix}, \quad (14)$$

where (u_0, v_0, w_0) is the center of the first loop projected on the rotated frame $(\hat{u}, \hat{v}, \hat{w})$ and is defined as

$$\begin{bmatrix} u_0 \\ v_0 \\ w_0 \end{bmatrix} = [T_z(\alpha_z, \beta_z)] \times \begin{bmatrix} 0 \\ 0 \\ -r_{coil}/2 \end{bmatrix} \quad (15)$$

Assuming the second current loop is linearly shifted and its center is at $C'_2(x_0, y_0, z_0)$, as shown by the loop on the right in Fig. 13. The generated field by the loop is then

$$\vec{B}_2 = \vec{B}(x - r_{coil}\Gamma_z \sin\psi_z, y - r_{coil}\Gamma_z \cos\psi_z, \\ z - r_{coil}D_z - r_{coil}/2), \quad (16)$$

where D_z is a normalized mismatch in the z-direction, Γ_z and ψ_z are the shifts of coil's center C'_2 along the y- and x-directions. In polar coordinates, the corresponding parameters can be defined as

$$D_z = z_0/r_{coil} \quad (17)$$

$$\Gamma_z = \frac{1}{r_{coil}}\sqrt{y_0^2 + x_0^2} \quad (18)$$

$$\psi_z = \cos^{-1}\frac{y_0}{\sqrt{y_0^2 + x_0^2}} \quad (19)$$

From equations (12) and (16), the magnetic field of the misaligned Helmholtz coil becomes

$$\vec{B}_{HH}(x, y, z) = G_z \times \vec{B}_1 + \vec{B}_2, \quad (20)$$

where G_z is the transpose of T_z, which projects the field back to the main frame $(\hat{x}, \hat{y}, \hat{z})$.

The homogeneity of the magnetic field along the z-direction is defined by equation (8).
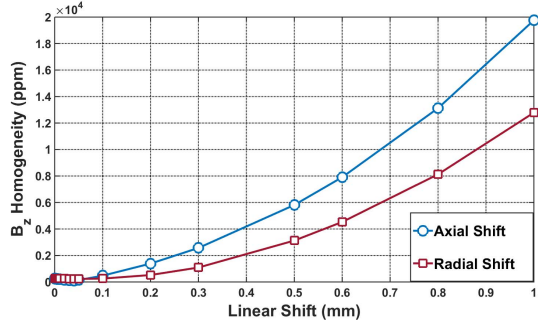
Fig. 14. Analytical modeling of folded Helmholtz coils' homogeneity as a function of the linear shift in the axial (circular markers) and radial (square markers) directions.
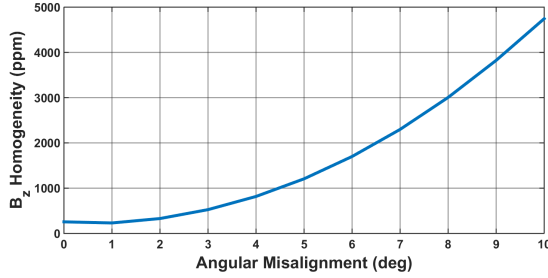

Fig. 15. Analytical modeling of folded Helmholtz coils' homogeneity as a function of the angular misalignment along the x and y axes.

The linear misalignment in the range from 0 to 1mm shows that the axial shift (along the z-axis) has a larger impact on the homogeneity than the radial shift (along the x- and y-axis), Fig. 14. The angular shifts α_z and β_z, on the other hand, show an identical effect on the field homogeneity in the z-direction, Fig. 15.

Folded coils are defined by the locking slots at the bottom side and a locking latch at the top side, visible in Fig. 4 and Fig. 9. These components are typically defined with a few microns of tolerance. The folding is accomplished using a pre-defined mold for guided assembly, Fig. 6. However, etching through a $500\mu m$ wafer introduces fabrication imperfections which could be up to $20\mu m$. This translates to 5 mrad angular misalignment or $20\mu m$ linear misalignment.

2) Projection of Imperfections to Performance: The resonance line width of Rb atoms in equations (4) and (5) is determined by the transverse relaxation time T_2, and they are related as [24],

$$\Delta\omega = \frac{1}{T_2} \tag{21}$$

Optical pumping, spin exchange, spin destruction, and wall collisions are all the factors that contribute to broadening the resonance line [38]. In addition, the field gradient inside the cell causes the Rb atoms to precess at different frequencies, which contribute to further broadening of the resonance line [24]. By lumping all factors, except for the field gradient, and calling it $\Delta\omega_{setup}$, we can write the measured resonance line width $\Delta\omega_m$ as

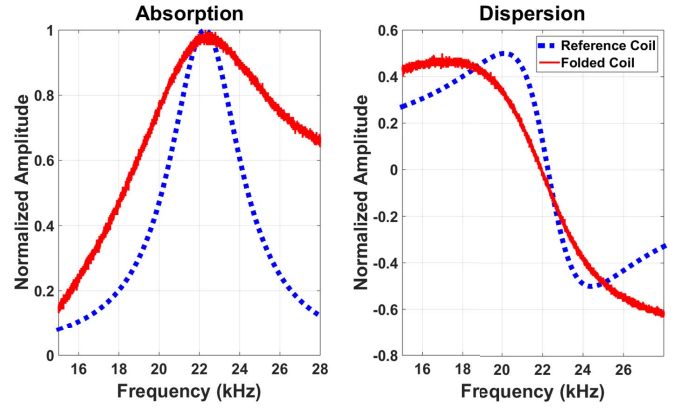$$\Delta\omega_m = \Delta\omega_{setup} + \Delta\omega_{gradient} \tag{22}$$

Fig. 16. Normalized absorption and dispersion curves (experimentally measured) of both the folded coil sample (solid red) and the reference coil (dashed blue).

Now that the $\Delta\omega_{gradient}$ is known, equation (21) gives the relaxation time associated with the field gradient. The field gradient is then defined as

$$\Delta B_z = \frac{1}{\pi \gamma T_{2,gradient}} \tag{23}$$

3) Experimental Results: The experimental evaluation of this model was performed using a folded coil sample with the radius $R_{coil} = 3$mm and a 2mm cubic cell. The sample was hand-folded which resulted in an angular, radial, and axial misalignments measured optically to be 5.2°, 0.87mm, and 0.6mm, respectively. The folded sample was placed inside a 4-layer magnetic shield with integrated 3 axes magnetic field coils (reference coils). The main field $B_0 = 4.7$ μT was applied along the z-axis, that is the pump beam axis, and an RF field was applied along the y-axis, which is the probe beam axis. The RF was swept from 15 kHz to 28 kHz to generate the Rb absorption and dispersion resonance lines.

First, the main field was applied using the reference coil to calculate $\Delta\omega_{setup}$ in equation (22), then repeated using the folded coil sample to estimate $\Delta\omega_{gradient}$. Fig. 16 shows the normalized experimental curves for both cases. It was found that the broadening due to the field gradient was around 846Hz, which corresponded to the field non-homogeneity of $\eta_{B_z(exp)} = 38585$ ppm, according to equation (8), (21) and (23). The analytically estimated magnetic field non-homogeneity was derived to be $\eta_{B_z(model)} = 37337$ ppm, which is in a close agreement to what was measured experimentally. This result correlates to the optimal case with $R_{coil} = 4.2$mm, N=5 turns, 1 mm cell. For the optimal case, we estimated non-homogeneity to be on the level of 345ppm.

B. Folded Backbone Structure

1) Analytical Model: The folded structure's panels in Fig. 17 are fabricated on the wafer-level (flat), then subsequently folded into 3D configuration. The folding procedure is performed by rotating panel 1 with respect to the base, panel 2 with respect to panel 1, and panel 3 with respect to panel 2, by utilizing three hinges marked as H1, H2, and
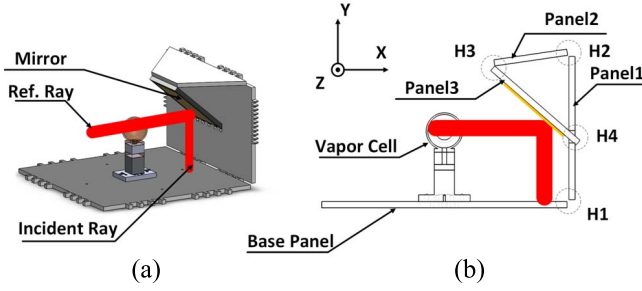
Fig. 17. Cross sectional view of Folded Structure (only the base panel and one side of the folded structure are shown for clarity).

TABLE I

ROTATION OF THE NORMAL VECTORS OF THE FOLDED STRUCTURE PANELS RELATIVE TO THE ADJACENT PANEL

Angle	Base-Panel1	Panel1-Panel2	Panel2-Panel3
ψ	90	109.5	115.5
θ	0	0	0
ϕ	0	0	0

H3 in Fig. 17. The rotation of each panel can be modeled using three Euler's angles (ψ: about the z-axis, θ: about the y-axis and, ϕ: about the x-axis). The orientations of the normal vectors of each panel are calculated using the directional cosine matrix (DCM) in equation (24).

$$\begin{bmatrix} \cos\theta\cos\psi & -\cos\phi\sin\psi & \sin\phi\sin\psi \\ & +\sin\phi\sin\theta\cos\psi & +\cos\phi\sin\theta\cos\psi \\ \cos\theta\sin\psi & \cos\phi\cos\psi & -\sin\phi\cos\psi \\ & +\sin\phi\sin\theta\sin\psi & +\cos\phi\sin\theta\cos\psi \\ -\sin\theta & \sin\phi\cos\theta & \cos\phi\cos\theta \end{bmatrix}, \tag{24}$$

To achieve 45° mirrors for the current design, the angles of panels relative to each other are summarized in Table I.

The normal unit vector to the base panel is defined as $\vec{v}_B = [0\ 1\ 0]'$. Thus, the normal unit vectors to the other corresponding panels are defined as

$$\vec{v}_1 = [DCM_{B,1}]\vec{v}_B, \tag{25}$$
$$\vec{v}_2 = [DCM_{1,2}]\vec{v}_1, \tag{26}$$
$$\vec{v}_3 = [DCM_{2,3}]\vec{v}_2, \tag{27}$$

where $[DCM_{i,j}]$ is the directional cosine matrix that describes the jth panel rotation relative to the ith panel. The normal unit vector to the mirror is $\vec{v}_m = -\vec{v}_3$ and the unit vector of the incident ray is $\vec{v}_I = \vec{v}_B$. The reflected ray's unit vector becomes

$$\vec{v}_R = [DCM_{I,R}]\vec{v}_I, \tag{28}$$

where the Euler's angles for the $[DCM_{I,R}]$ are ($\psi_{I,R} = \pi - 2(\pi - \beta)$, $\theta_{I,R} = 0$ and, $\phi_{I,R} = \pi/2 - \gamma$). β and γ are the angles made by the mirror's unit vector and the y- and z-axis respectively, Fig. 17.

Latches on the sidewalls (panels) of the folded structure ensure the proper alignment of the structure's parts with respect to each other. Similar to the folding process of

coils, a predefined mold would be used for folding and permanent enforcement. Since the NMR sensors operation requires heating the cell, a potential misalignment might occur due to thermal expansion of the enforcement material. Our study of different enforcement materials on similar structures concluded that the effect of enforcement material's thermal expansion is inversely proportional to the size of the folded structure [39].

For example, the coefficient of thermal expansion (CTE) of an AuSn alloy is 16 PPM/°C, a 100°C temperature difference would result in 0.16% volume expansion of the enforcement material. Since the hinge volume is 2mm^3, and assuming there is 20% more alloy on one of the hinges between the base and panel 1, the excess would result in 6.3mrad misalignment of panel 1 relative to the base panel, which is translated to 50μm misalignment of the beam with respect to the cell, according to equations (25)-(28).

2) Projection of Imperfections to Performance: Displacement of the pump beam would result in reduction of the pumping rate, which would reduce the number of polarized Rb atoms. Misalignment of the probe, on the other hand, reduces the number of interrogated atoms. Both scenarios result in a drop of the signal-to-noise ratio (SNR). Since the used beams for pumping and probing are Gaussian beams, the drop in SNR is expected to follow the Gaussian function:

$$y = ae^{-x^2/2c^2}, \tag{29}$$

where y is the SNR of the magnetometer, a is the SNR value in the perfectly aligned state, x is the displacement of the beam relative to the cell, c is the width of the Gaussian curve which determines the relation between the SNR decay and the beam displacement.

3) Experimental Results: To verify experimentally the effect of reflector misalignment with respect to the cell, a sample reflector of the folded structure was placed on a 6-axis optical mount and its angle was controlled to create a displacement of the light beams (pump and probe) relative to a 2mm cell. Fig. 18 illustrates the experimental setup. Fig. 19 shows the relationship of the normalized magnetometer's sensitivity to displacement of the beam. As predicted by the model, the drop in the magnetometer sensitivity follows the Gaussian function. We found that SNR is more sensitive to the probe beam displacement than to the pump beam. This is explained by the optical power on the pump beam to be higher than the probe beam.

VI. PREDICTION OF PERFORMANCE

As discussed in previous sections, the folding error can be either due to the folded coils, which affects the relaxation time T_2 of Xe atoms, or due to the folded structure, which affects the Signal-to-Noise Ratio (SNR) of the electron paramagnetic resonance (EPR) magnetometer [40].

Assuming a closed loop system with the white noise limiting the photo-detector, the Angle Random Walk (ARW) of the NMRG is predicted by the relatio [41],

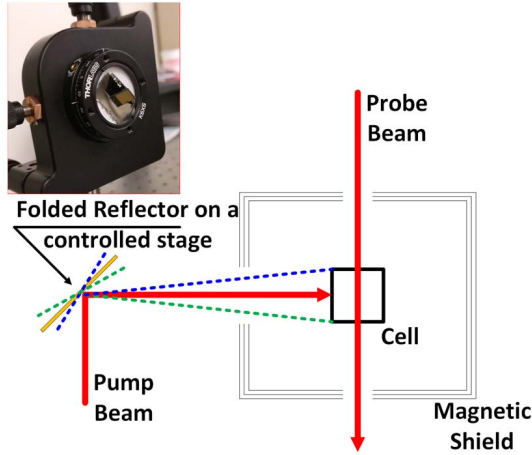$$ARW = \frac{3600}{T_2 \times SNR\sqrt{\Delta f}}[°/\sqrt{hr}], \tag{30}$$

Fig. 18. Sketch illustrating the experimental setup used for measuring the effect of pump beam displacement relative to the cell on the magnetometer sensitivity.
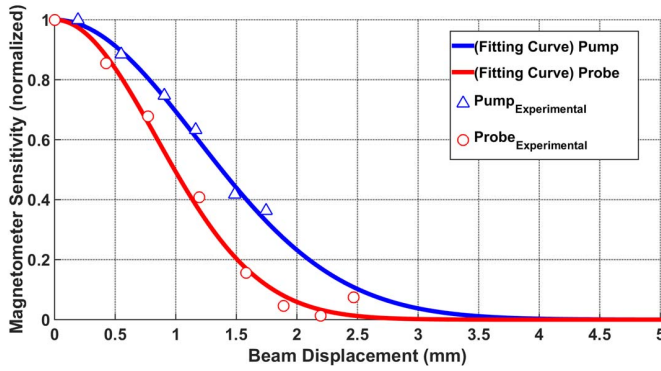

Fig. 19. Normalized Magnetometer Sensitivity (experimentally measured) vs beams displacement relative to the cell (pump: triangles, probe: circles).
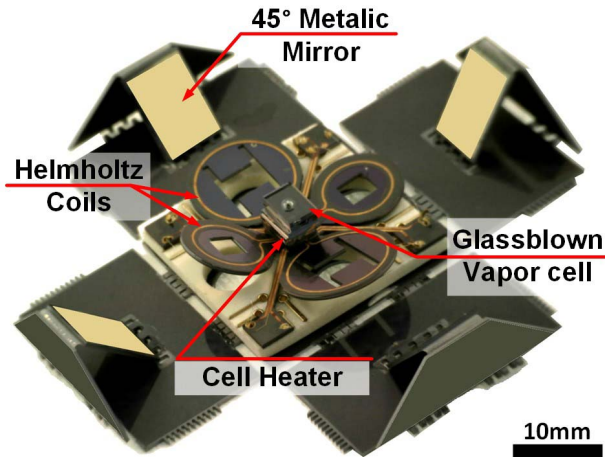

Fig. 20. Partially folded NMR sensor prototype showing all components of the system.

where T_2 is the transverse relaxation time, SNR is the signal to noise ratio, Δf is the bandwidth of the phase noise in Hz.

On the other hand, the fundamental sensitivity limit of the NMRM is related to two factors, EPR magnetometer SNR and
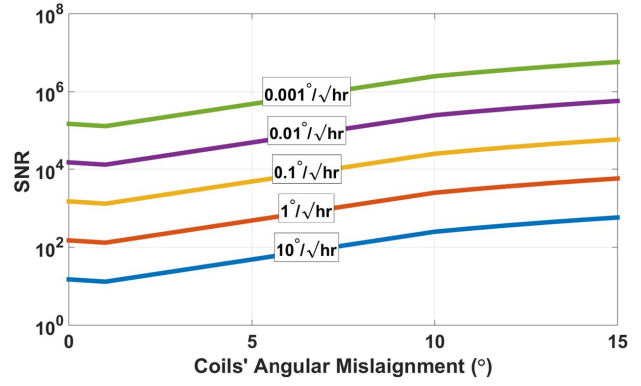

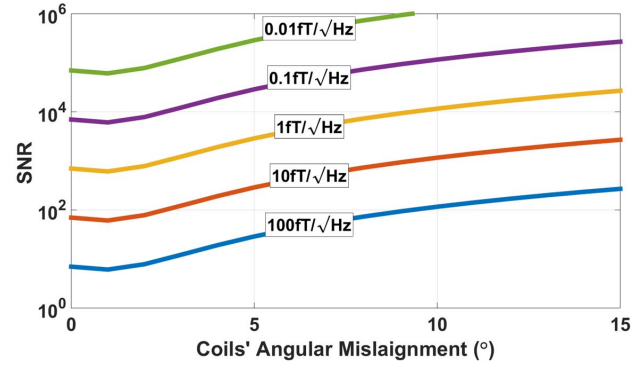Fig. 21. NMRG ARW as a function of SNR and coils' angular misalignment.

Fig. 22. NMRM sensitivity as a function of SNR and coils' angular misalignment.

Xe atoms relaxation time T_2. The fundamental sensitivity can be defined as [40],

$$\delta B_n = \frac{1}{2\pi \gamma T_2} \times \frac{\delta B_e}{P \times dB_n/dP},\qquad (31)$$

where δB_e is the noise floor of the EPR magnetometer, P is the percentage of polarized Xe atoms, dB_n/dP is the magnetic field produced by Xe atoms per unit polarization.

The fundamental sensitivity of EPR magnetometer of a cell with an internal diameter of 1mm containing Rubidium and a buffer gas is limited by the atomic shot noise to approximately $120fT/\sqrt{Hz}$ [24].

Assuming ^{129}Xe transverse relaxation time $T_2 = 20s$, the effect of the angular misalignment of the coils on the NMRG ARW and the NMRM fundamental sensitivity is presented by Fig. 21 and Fig. 22, respectively. Similarly, curves with circular markers in Fig. 23 and Fig. 24 represent NMRG ARW and NMRM sensitivity, respectively, due to linear axial misalignments, while the curves with triangular markers in Fig. 23 and Fig. 24 represent linear radial misalignments. The general trend in both figures is that as the misalignment increases the required SNR to achieve a certain ARW value increases. For example, SNR of 150 can achieve $\sim 1°/\sqrt{hr}$ with perfectly aligned coils, while 5° angular misalignment increases the SNR requirement by a factor of 4 to achieve the same $1°/\sqrt{hr}$.

To visualize the impact of the folded structure misalignment on the device performance, we assumed a constant
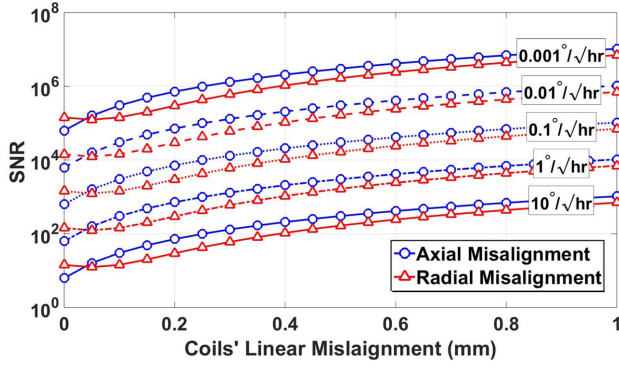
Fig. 23. NMRG ARW as a function of SNR and coils' linear misalignment (axial: circular markers, radial: triangular markers).
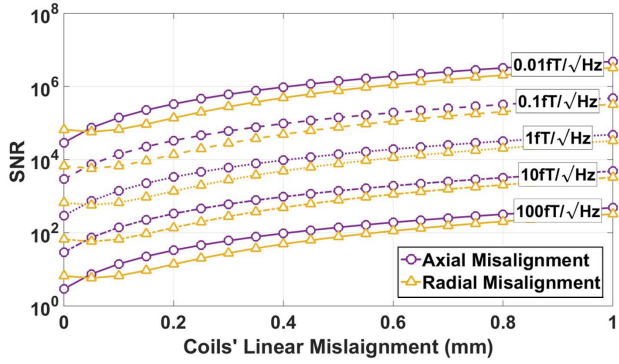

Fig. 24. NMRM sensitivity as a function of SNR and coils' linear misalignment (axial: circular markers, radial: triangular markers).
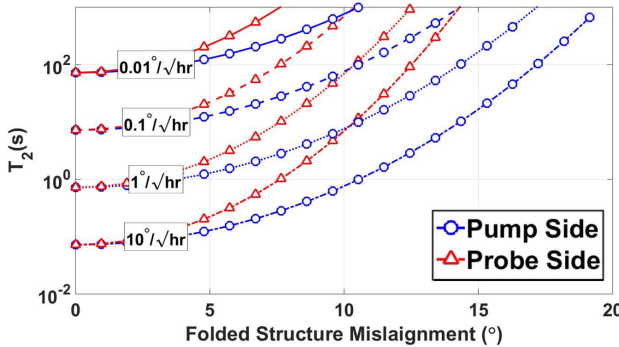

Fig. 25. NMRG ARW as a function of Relaxation time (T_2) and Folded Structure misalignment (Pump: circular markers, Probe: triangular markers).

SNR=5000. Using equations (30), (31) and extrapolating the experimental points presented by Fig. 19, the NMRG ARW and NMRM sensitivity are depicted by Fig. 25 and Fig. 26, respectively, under different combinations of the relaxation time (T_2) and the folded structure misalignment. The curves with circular markers of Fig. 25 and Fig. 26 represent cases when the misalignment occurs on the pump side and the curves with triangular markers are on the probe side of NMRG and NMRM, respectively.

The developed error model and the phenomenological analytical model suggests that the introduced design with 5mrad angular misalignment between the coils and the folded mirrors and 100μm linear misalignment between folded coils can
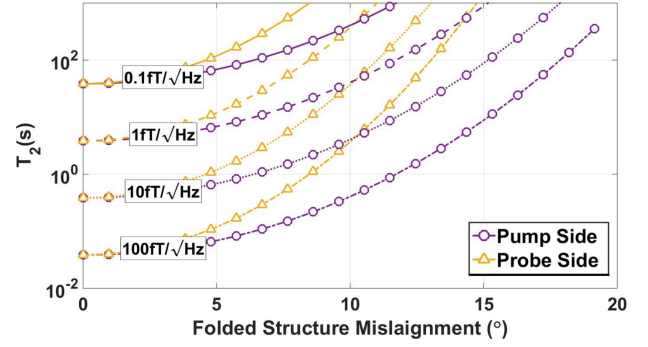

Fig. 26. NMRM sensitivity as a function of Relaxation time (T_2) and Folded Structure misalignment (Pump: circular markers, Probe: triangular markers).

achieve NMRG's ARW ~0.1°$\sqrt[]{hr}$ and NMRM fundamental sensitivity better than 10 fT$\sqrt[]{Hz}$.

VII. CONCLUSION

We presented an approach for implementation of MEMS components for NMR sensors utilizing a batch fabrication process, with minimum assembly requirements. We evaluated the performance boundaries of our suggested design by estimating possible fabrication imperfections and projected their effect on the device performance. Our error analysis method is general and could be applied to other implementations. The analysis suggested that the presented folded MEMS approach is a strong candidate for implementation of at least a tactical-grade level of performance micro-NMRG and a femto-Tesla level of performance micro-NMRM.

REFERENCES

[1] R. M. Noor, V. Gundeti, and A. M. Shkel, "A status on components development for folded micro NMR gyro," in *Proc. IEEE Int. Symp. Inertial Sensors Syst. (INERTIAL)*, Kauai, HI, USA, Mar. 2017, pp. 156–159.

[2] J. Kitching, S. Knappe, and E. A. Donley, "Atomic sensors—A review," *IEEE Sensors J.*, vol. 11, no. 9, pp. 1749–1758, Sep. 2011.

[3] I. K. Kominis, T. W. Kornack, J. C. Allred, and M. V. Romalis, "A subfemtotesla multichannel atomic magnetometer," *Nature*, vol. 422, no. 6932, pp. 596–599, 2003.

[4] L. K. Lam, E. Phillips, E. Kanegsberg, and G. W. Kamin, "Application of CW single-mode GaAlAs lasers to Rb-Xe NMR gyroscopes," *Proc. SPIE*, vol. 412, pp. 272–277, Sep. 1983.

[5] A. M. Shkel, "The chip-scale combinatorial atomic navigator," *GPS World*, vol. 24, no. 8, pp. 8–10, 2013.

[6] H. Korth *et al.*, "Miniature atomic scalar magnetometer for space based on the rubidium isotope [87]Rb," *J. Geophys. Res., Space Phys.*, vol. 121, no. 8, pp. 7870–7880, 2016.

[7] H. C. Abbink, E. Kanegsberg, K. D. Marino, and C. H. Volk, "Micro-cell for NMR gyroscope," U.S. Patent 7 292 031, Nov. 6, 2007.

[8] E. J. Eklund, A. M. Shkel, S. Knappe, E. Donley, and J. Kitching, "Glass-blown spherical microcells for chip-scale atomic devices," *Sens. Actuators A, Phys.*, vol. 143, no. 1, pp. 175–180, 2008.

[9] M. A. Perez, U. Nguyen, S. Knappe, E. A. Donley, J. Kitching, and A. M. Shkel, "Rubidium vapor cell with integrated Bragg reflectors for compact atomic MEMS," *Sens. Actuators A, Phys.*, vol. 154, no. 2, pp. 295–303, 2009.

[10] W. C. Griffith, S. Knappe, and J. Kitching, "Femtotesla atomic magnetometry in a microfabricated vapor cell," *Opt. Express*, vol. 18, no. 26, pp. 27167–27172, 2010.

[11] D. K. Serkland *et al.*, "VCSELs for atomic sensors," Sandia Nat. Lab., Albuquerque, NM, USA, Tech. Rep. SAND2007-0681C, 2007.

[12] S. A. Knappe, "Emerging topics: MEMS atomic clocks," in *Comprehensive Microsystems*, vol. 3. Amsterdam, The Netherlands: Elsevier, 2007.

[13] S. Knappe, O. Alem, D. Sheng, and J. Kitching, "Microfabricated optically-pumped magnetometers for biomagnetic applications," *J. Phys., Conf. Ser.*, vol. 723, no. 1, pp. 012055-1–012055-6, 2016.

[14] R. Jiménez-Martínez and S. Knappe, "Microfabricated optically-pumped magnetometers," in *High Sensitivity Magnetometers*. Cham, Switzerland: Springer, 2017, pp. 523–551.

[15] J. Kitching, E. A. Donley, E. Hodby, A. Shkel, and E. J. Eklund, "Compact atomic magnetometer and gyroscope based on a diverging laser beam," U.S. Patent 7 872 473, Jan. 18, 2011.

[16] L. M. Lust and D. W. Youngner, "Chip scale atomic gyroscope," U.S. Patent 7 359 059, Apr. 15, 2008.

[17] H. C. Abbink, E. Kanegsberg, and R. A. Patterson, "NMR gyroscope," U.S. Patent 7 239 135, Jul. 3, 2007.

[18] E. J. Eklund, A. M. Shkel, S. Knappe, E. Donley, and J. Kitching, "Spherical rubidium vapor cells fabricated by micro glass blowing," in *Proc. IEEE Conf. Micro Electro Mech. Syst. (MEMS)*, Kobe, Japan, Jan. 2007, pp. 171–174.

[19] M. A. Perez, J. Kitching, and A. M. Shkel, "Design and demonstration of PECVD multilayer dielectric mirrors optimized for micromachined cavity angled sidewalls," *Sens. Actuators A, Phys.*, vol. 155, no. 1, pp. 23–32, 2009.

[20] S. Knappe *et al.*, "A microfabricated atomic clock," *Appl. Phys. Lett.*, vol. 85, no. 9, pp. 1460–1462, 2004.

[21] M. Larsen and M. Bulatowicz, "Nuclear magnetic resonance gyroscope: For DARPA's micro-technology for positioning, navigation and timing program," in *Proc. IEEE Int. Symp. Inertial Sensors Syst. (ISISS)*, Laguna Beach, CA, USA, May 2014, pp. 1–5.

[22] R. Mhaskar, S. Knappe, and J. Kitching, "A low-power, high-sensitivity micromachined optical magnetometer," *Appl. Phys. Lett.*, vol. 101, no. 24, p. 241105, 2012.

[23] S. A. Zotov, M. C. Rivers, A. A. Trusov, and A. M. Shkel, "Chip-scale IMU using folded-MEMS approach," in *Proc. IEEE Sensors Conf.*, Waikoloa, HI, USA, Nov. 2010, pp. 1043–1046.

[24] E. J. Eklund, "Microgyroscope based on spin-polarized nuclei," Ph.D. dissertation, Dept. Elect. Eng. Comput. Sci., Univ. California, Irvine, Irvine, CA, USA, 2008.

[25] N. J. Stone, "Table of nuclear magnetic dipole and electric quadrupole moments," *Atomic Data Nucl. Data Tables*, vol. 90, no. 1, pp. 75–176, 2005.

[26] T. G. Walker and W. Happer, "Spin-exchange optical pumping of noble-gas nuclei," *Rev. Mod. Phys.*, vol. 69, no. 2, p. 629, 1997.

[27] B. C. Grover, E. Kanegsberg, J. G. Mark, and R. L. Meyer, "Nuclear magnetic resonance gyro," U.S. Patent 4 157 495, Jun. 5, 1979.

[28] F. Bloch, "Nuclear induction," *Phys. Rev.*, vol. 70, nos. 7–8, p. 460, 1946.

[29] Y. Liu, J. K. Boyles, J. Genzer, and M. D. Dickey, "Self-folding of polymer sheets using local light absorption," *Soft Matter*, vol. 8, no. 6, pp. 1764–1769, 2012.

[30] R. Mohr, K. Kratz, T. Weigel, M. Lucka-Gabor, M. Moneke, and A. Lendlein, "Initiation of shape-memory effect by inductive heating of magnetic nanoparticles in thermoplastic polymers," *Proc. Nat. Acad. Sci. USA*, vol. 103, no. 10, pp. 3540–3545, 2006.

[31] S. M. Felton *et al.*, "Self-folding with shape memory composites," *Soft Matter*, vol. 9, no. 32, pp. 7688–7694, 2013.

[32] R. Robbins. *SCS Parylene Deposition Standard Operating Procedure*. Accessed: Dec. 7, 2016. [Online]. Available: https://research.utdallas.edu/cleanroom/manuals/scs-parylene-deposition

[33] V. M. Gundeti, "Folded MEMS approach to NMRG," M.S. thesis, Dept. Mater. Manuf. Technol., Univ. California Irvine, Irvine, CA, USA, 2015.

[34] M. D. Bulatowicz, "Temperature system with magnetic field suppression," U.S. Patent 8 138 760, Mar. 20, 2012.

[35] L. Nieradko *et al.*, "New approach of fabrication and dispensing of micromachined cesium vapor cell," *J. Micro/Nanolithogr., MEMS, MOEMS*, vol. 7, no. 3, p. 033013, 2008.

[36] E. J. Eklund and A. M. Shkel, "Glass blowing on a wafer level," *J. Microelectromech. Syst.*, vol. 16, no. 2, pp. 232–239, Apr. 2007.

[37] R. Beiranvand, "Analyzing the uniformity of the generated magnetic field by a practical one-dimensional Helmholtz coils system," *Rev. Sci. Instrum.*, vol. 84, no. 7, p. 075109, 2013.

[38] I. M. Savukov, "Spin exchange relaxation free (SERF) magnetometers," in *High Sensitivity Magnetometers*. Cham, Switzerland: Springer, 2017, pp. 451–491.

[39] Y.-W. Lin, A. Efimovskaya, and A. M. Shkel, "Study of environmental survivability and stability of folded MEMS IMU," in *Proc. IEEE Int. Symp. Inertial Sensors Syst. (INERTIAL)*, Kauai, HI, USA, Mar. 2017, pp. 132–135.

[40] M. Bulatowicz and M. Larsen, "Compact atomic magnetometer for global navigation (NAV-CAM)," in *Proc. IEEE/ION Position Location Navigat. Symp. (PLANS)*, Myrtle Beach, SC, USA, Apr. 2012, pp. 1088–1093.

[41] I. A. Greenwood and J. H. Simpson, "Fundamental noise limitations in magnetic resonance gyroscopes," in *Proc. Nat. Aerosp. Electron. Conf. (NAECON)*, Dayton, OH, USA, May 1977, pp. 1246–1250.

Radwan M. Noor (S'17) received the B.Sc. degree in electrical engineering from King Abdulaziz University, Jeddah, Saudi Arabia, in 2008, and the M.Sc. degree in electrical engineering from the University of Southern California, Los Angeles, in 2014. He is currently pursuing the Ph.D. degree in electrical engineering and computer science with a focus on microelectromechanical systems (MEMS) in association with the Microsystems Laboratory, University of California at Irvine, Irvine. He is also a Graduate Student Research Assistant with the Microsystems Laboratory, University of California at Irvine. His research interests include the design, modeling, and fabrication of solid-state and atomic MEMS inertial sensors.

Andrei M. Shkel (F'99) received the Diploma degree (Hons.) in mechanics and mathematics from Moscow State University, Moscow, Russia, in 1991, and the Ph.D. degree in mechanical engineering from the University of Wisconsin–Madison, Madison, WI, USA, in 1997. In 2000, he joined the faculty of the University of California at Irvine, Irvine, CA, USA, where he is currently a Professor with the Department of Mechanical and Aerospace Engineering, with a joint appointment in the Department of Electrical Engineering and Computer Science and the Department of Biomedical Engineering. He served as the Program Manager of the Microsystems Technology Office, Defense Advanced Research Projects Agency, Arlington, VA, USA, from 2009 to 2013. His professional interests are reflected in over 200 publications. He holds over 40 U.S. patents. His current interests include the design, manufacturing, and advanced control of precision micromachined gyroscopes. He was a recipient of the 2002 George E. Brown, Jr., Award, the 2005 NSF CAREER Award, the 2006 UCI HSSoE Best Faculty Research Award, and the 2009 IEEE Sensors Council Technical Achievement Award. In 2013, he received the Office of the Secretary of Defense Medal for Exceptional Public Service. He has served on a number of editorial boards, most recently, as an Editor of the IEEE/ASME JOURNAL OF MICROELECTROMECHANICAL SYSTEMS, an Associate Editor-in-Chief of the IEEE SENSORS LETTERS, an Editorial Board Member of the *Journal of Gyroscopy and Navigation*, and the Founding Chair of the IEEE International Symposium on Inertial Sensors and Systems. He was voted the 2018 President-Elect of the IEEE Sensors Council.